Understanding the interlayer coupling in $1T/1H$-$NbSe_2$ heterobilayers

Roman Pico,* Paula Abufager,† and Ignacio Hamad

Instituto de Física de Rosario, Consejo Nacional de Investigaciones Científicas y Técnicas (CONICET) and Facultad de Ciencias Exactas, Ingeniería y Agrimensura. Universidad Nacional de Rosario, 27 de Febrero 210 Bis (2000) Rosario, Argentina

Roberto Robles and Nicolas Lorente

Centro de Física de Materiales CFM/MPC (CSIC-UPV/EHU), Paseo Manuel de Lardizabal 5, San Sebastián 20018, España

(Received 1 March 2024; revised 20 July 2024; accepted 2 August 2024; published 26 August 2024)

The properties of 2D materials are strongly influenced by their substrate, leading to a variety of proximity effects like screening, charge transfer, and hybridization. Surprisingly, there is a dearth of theoretical studies on these effects. Particularly, previous theoretical research on the star of David (SOD) structure in $1T$-$NbSe_2$ has focused on single-layer configurations or stacking with the same $1T$ phase without any real substrate. Here, we depart from these approaches and explore how these proximity effects shape the electronic and magnetic properties of the $1T$-$NbSe_2$ phase when it is grown on the metallic $1H$-$NbSe_2$ substrate. Using density functional calculations, we establish a common framework to define the key characteristics of both free-standing $1T$-$NbSe_2$ and $1H$-$NbSe_2$. We then identify the optimal stacking arrangement for these two layers, revealing a transfer from the $1T$ to the $1H$ phase and a reorganization of charge within each layer. Our findings indicate that the magnetic moment of the SOD structure is still robust; however, it is diminished due to a reduction in the on-site Coulomb interaction of the Hubbard bands. Additionally, the interlayer coupling induces metallicity in the $1T$ phase and increases the decoupling of the lower Hubbard band from the valence band.

DOI: 10.1103/PhysRevB.110.075427

I. INTRODUCTION

In recent years, two-dimensional (2D) van der Waals (vdW) materials, particularly transition metal dichalcogenides (TMDs), have captured the attention of the scientific community [1,2]. These materials, heralded for their versatile applications in optoelectronic and spintronic technologies, offer a unique playground for material engineering and device fabrication [3]. Among TMDs, like TaS_2 [4–8], $TaSe_2$ [9–11], or NbS_2 [12,13], $NbSe_2$ is a prominent example, showcasing a spectrum of electronic phases such as charge density wave (CDW), superconductivity, and variable electronic structures in its different phases like single layers (SLs) of the $1H$ and $1T$ phases [14–18]. The $1T$ phase of $NbSe_2$, distinct from the $1H$ phase in terms of symmetry and electronic properties, adds an extra layer of complexity and potential to these materials, paving the way for tailoring the overall properties of the system through phase engineering. While the $1H$ phase is a metal, that at low temperatures ($T_c = 7.2$K for bulk and $T_c = 3.2$K for the monolayer [14,19–22]) develops superconductivity, the $1T$ was initially identified as a Mott insulator [23], but, however, it has recently been characterized as a charge transfer (CT) insulator [18].

The interplay between the $1H$ and $1T$ phases in heterolayers of $NbSe_2$ enriches its physical properties, allowing for the manipulation of electronic and spin states in unique ways. This ability to tailor the characteristics of TMDs by controlling their phase composition opens avenues for customized material properties, particularly in the context of proximity effects in heterostructures and their applications in advanced technologies [24].

More recently, magnetic impurities have been deposited on clean surfaces of $2H$-$NbSe_2$, resulting in the appearance of Yu-Shiba-Rusinov (YSR) bound states in the superconducting gap [25]. This could be linked to the creation of a topological phase and Majorana bound states. The experimental exploration of the vertically stacked $1T$ and $1H$ $NbSe_2$ layers (hereafter referred to as $1T/1H$) has unveiled intriguing phenomena that occur at the interface of these two phases. When the $1T$ phase is combined with the $1H$ phase, distinct and noteworthy effects have been observed, such as the emergence of YSR bound states and Kondo resonances within the superconducting gap [18]. These effects highlight the complex and unique interactions at the $1T/1H$ interface, showcasing how the combination of different phases can lead to unique physical behaviors.

These experimental results suggest a significant modification of electronic and magnetic properties at the interface. This modification indicates an underlying influence that could be akin to a proximity effect [26], where the presence of one phase impacts the properties of the adjacent phase. These findings are pivotal in understanding the coupled dynamics of the $1T$ and $1H$ phases and offer valuable insights into the potential mechanisms driving their interaction. This experimental backdrop forms an important context for our theoretical study.

*Contact author: pico@ifir-conicet.gov.ar
†Contact author: abufager@ifir-conicet.gov.ar

From the theoretical point of view and within the framework of calculations based on density functional theory (DFT), the simultaneous description of monolayers in 1*H* and 1*T* phases of $NbSe_2$ is a great challenge due to the different physical characteristics that each of them presents. Consequently, different approximations are utilized in their computational treatment to address this complexity and enhance the overall accuracy of the theoretical framework [16,18,27,28]. This challenge likely explains the lack of theoretical studies devoted to understanding the interaction between 1*T* and 1*H* or 2*H* layers, as well as the behavior of the magnetic moment of the 1*T* layer when it is in contact with the 1*H* phase—an aspect crucial for the occurrence of the Kondo effect reported in experiments. Our paper aims to go beyond these studies by exploring the interaction between 1*T* and 1*H* layers in greater detail.

In this theoretical work, we intend to simultaneously capture the main features of both phases from DFT calculations finding a common set of parameters such as lattice constant and effective on-site Coulomb interaction (U_{eff}), that correctly describe both phases. Then we shift our focus towards exploring the interactions at the interlayer interface. This exploration is crucial for understanding how the distinct properties of each phase influence each other when combined in a heterostructure. We investigate the nuances of interlayer coupling, particularly how it affects the electronic and magnetic properties of the combined system. This part of our paper aims to provide deeper insight into the synergistic effects at play between the 1*H* and 1*T* phases, shedding light on the potential of these interactions to induce unique phenomena in $NbSe_2$ heterostructures.

II. METHODS

Spin-polarized DFT calculations were performed with the VASP code [29–34] within the slab-supercell approach and using the projector augmented-wave method [33]. Wave functions were expanded using a plane-wave basis set with an energy cutoff of 500 eV. We used the Perdew-Burke-Ernzerhof (PBE) functional [35] to treat the exchange-correlation energy. We added the missing van der Waals interactions using the Tkatchenko-Scheffler scheme [36]. The strongly-correlated correction is considered with the DFT + *U* approach [37] to deal with the Nb *d* electrons. In this paper, we investigated the influence of varying U_{eff} values for Nb(*d*) atoms on the lattice constant, electronic properties, and magnetic properties of isolated 1*T* and 1*H* monolayers (see Supplemental Material (SM) [38]). Furthermore, we used linear response theory [39] to estimate an optimal U_{eff} value for both monolayers. Overall, this approach allowed us to analyze the interplay between electronic structure, magnetic behavior, and lattice constants, providing valuable insights into the properties of these materials. The HSE06 hybrid functional was tested to describe the physical properties of the 1*H* and 1*T* monolayers. However, it was found to incorrectly characterize the metallic and insulating properties of the 1*H* and 1*T* phases, respectively. These findings are consistent with some theoretical results previously reported [40]. The isolated monolayers of 1*H* and 1*T* were studied using 1×1 and $\sqrt{13} \times \sqrt{13}$ unit cells. Test calculations for the 3×3 CDW of the 1*H* phase revealed that our primarily conclusions remain unchanged, even when considering a 1×1 unit cell. The 3×3 CDW in $NbSe_2$ is weak and does not significantly alter the band structure or density of states (DOS). For the heterobilayer 1*T*/1*H*, a $\sqrt{13} \times \sqrt{13}$ unit cell was used. It is worth mentioning that incorporating a commensurate unit cell for the CDW of both 1*T* and 1*H* layers would need an unfeasibly large supercell. The $4p^6 4d^4 5s^1$ states of Nb atoms and the $4s^2 4p^4$ states of Se atoms are treated as valence states. For ionic relaxation, we used a $13 \times 13 \times 1$ and $3 \times 3 \times 1$ k-grids for 1×1 and $\sqrt{13} \times \sqrt{13}$, respectively. For the projected density of states (PDOS), we used a $100 \times 100 \times 1$ and $18 \times 18 \times 1$ k-grids for 1×1 and $\sqrt{13} \times \sqrt{13}$, respectively.

To analyze the charge transfer process, we employed the Bader scheme [41] to calculate the charge in the 1*T*/1*H*, 1*T* and 1*H* optimal structures. To gain further insights, we also computed the difference between the charge densities of the entire 1*T*/1*H* model and the separated 1*T* and 1*H* layers, denoted as $\Delta\rho = \rho_{1T/1H} - \rho_{1T} - \rho_{1H}$. Here, $\rho_{1T/1H}$, ρ_{1T}, and ρ_{1H} refer to the charge densities of the whole 1*T*/1*H* system, the 1*T* layer, and the 1*H* layer, respectively. To obtain ρ_{1T} and ρ_{1H}, we removed the 1*H* monolayer and the 1*T* layers from the entire system respectively, while keeping the remaining atomic structures unchanged. While for the 1*H*/1*H* phase [42] spin orbit coupling (SOC) is important at the superconductivity energy scale, it does not have a significant effect at the electronic energy scale, the one we are interested in. Moreover, for the 1*T* phase, SOC was shown to have a minor effect [28]. Since our focus is on the 1*T* phase at the bilayer, the inclusion of SOC would increase the already high computational cost without significant modifications in the presented results.

III. RESULTS AND DISCUSSION

A. Single layers of 1*T* and 1*H* $NbSe_2$

Single layers of 1*H*-$NbSe_2$ consist of hexagonal arrangements of Nb atoms enveloped within a trigonal prismatic Se atom environment (see Fig. 1). Prior theoretical investigations have highlighted various atomic structures that are compatible with the 3×3 CDW distortions [16,17,43–47], and some of these alternatives exist within a narrow energy range of approximately 3 meV per formula unit [16]. This intriguing observation suggests a coexistence of these structures. Moreover, the deviations in atomic positions from the ideal 1×1 arrangement are relatively minor [16]. These findings collectively illuminate the complex interplay between structural modifications and electronic behaviors within the intricate landscape of 1*H*-$NbSe_2$. When it comes to the role of magnetism in 1*H*-$NbSe_2$, the exact nature of this phase is not clear [16,27,48]. .

Regarding the 1*T*-NbSe2 phase, monolayers and few layers [49] are, so far, experimentally accessible using molecular beam epitaxy [18,23,26,50,51]. The SL 1*T*-NbSe2 phase is characterized by a distinctive star of David (SOD) CDW pattern with a $\sqrt{13} \times \sqrt{13}$ periodicity [23]. Within this CDW pattern, each SOD comprises 12 outer Nb atoms that undergo contraction toward a central Nb atom. Additionally, six Se atoms are positioned in the upper plane and six in the lower

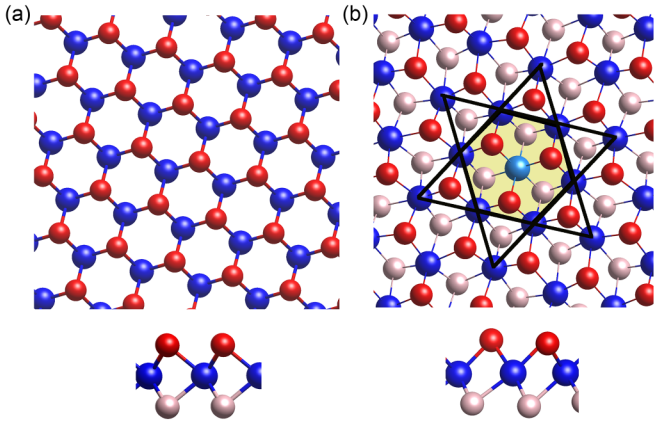

FIG. 1. Structure of (a) 1*H* and (b) 1*T* single-layer configurations of $NbSe_2$. In these diagrams, blue spheres represent Nb atoms and red (pink) spheres represent Se atoms in the top (bottom) layers of the arrangement. The central region (CR) of the SOD within the 1*T* structure is indicated by the yellow shading. This region prominently features the central Nb atom (Nb_c), depicted as a cyan sphere, which is at the heart of the SOD. Surrounding Nb atoms that are in close proximity to Nb_c are represented as blue spheres (hereafter referred to as Nb_1). The pink Se atoms inside this area are named, Se_c and the ones outside are Se_o (see Fig. S1 [38] in the SM for visualization of the $\sqrt{13} \times \sqrt{13}$ unit cell of the 1*T* structure).

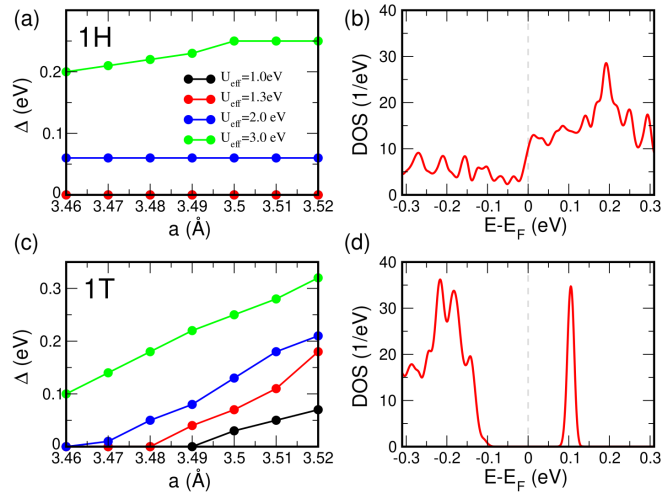

FIG. 2. Effect of the lattice constant, a (Å), on the band gap Δ (eV), of (a) 1*H*- and (c) 1*T* $NbSe_2$ monolayers with PBE+U (U_{eff}=1, 1.3, 2, and 3 eV). Density of states (DOS) calculated with U_{eff}=1.3 eV and $a = 3.52$ Å for (b) 1*H*- and (d) 1*T*- $NbSe_2$ monolayers. In (a), the red and black lines are overlapping. For the 1*H*-monolayer, the equilibrium lattice constant is 3.49 Å for U_{eff} values of 1 eV, 1.3 eV, and 2 eV, while it becomes 3.51 Å when U_{eff} is 3 eV. On the other hand, for the 1*T* monolayer, the equilibrium lattice constants are 3.49 Å, 3.50 Å, 3.51 Å, and 3.52 Å for U_{eff} values of 1 eV, 1.3 eV, 2 eV, and 3 eV, respectively.

plane of each SOD, as visually depicted in Fig. 1. In contrast to the 1*H* polytype, in the 1*T* phase, each Nb atom achieves octahedral coordination with its neighboring Se atoms. 1*T*-$NbSe_2$ has been characterized as a CT [18] in which the valence band (VB), mainly composed of the Se p_z states, appreciably hybridizes with the lower Hubbard band (LHB) [50,52]. It is important to mention that Liu *et al.* [18] demonstrated that the 1*T*/1*T*-$NbSe_2$ monolayer grown on highly oriented pyrolytic graphite (HOPG) exhibited an insulating state, indicating that the gap is not due to CDW stacking. Further investigations suggest that the gap's origin is complex, involving both local and long-range Coulomb interactions rather than just CDW order or nonlocal exchange [40]. Other studies have proposed that the insulating state results from a cooperative effect of lattice and magnetic interactions that enhance the Mott gap, as well as strong electron correlations that open a charge gap [18,28]. Therefore, in the case of the monolayer, both electronic correlations and intrinsic CDW contribute to the insulating gap. Our analysis will incorporate both of these mechanisms to describe the insulating state in the 1*T* phase.

In light of our ultimate objective, which centers on the comprehensive investigation of the physical characteristics exhibited by bilayer configurations composed of 1*T* and 1*H* stacked structures, it becomes paramount to establish a singular computational approach capable of encapsulating their salient attributes. Of particular significance is the determination of a unique lattice constant and the appropriate choice of the U_{eff} parameter for the treatment of Nb(4*d*) electrons. These parameters are pivotal not only in rendering an accurate representation of the metallic and insulating characteristics intrinsic to 1*H* and 1*T* single layers but also in elucidating their magnetic properties.

For the 1*H* SL, the variation of the band gap, denoted as Δ, with respect to the lattice constant is depicted in Fig. 2(a) for different values of U_{eff}. As expected, for high enough values of the Hubbard parameter, $U_{\text{eff}} \geqslant 2$ eV, the system becomes an insulator. Additionally, due to the presence of an odd number of electrons within the unit cell, the total magnetic moment is $M_T = 1\mu_B$ when the system becomes an insulator. An intriguing observation to note is that, for a fixed value of U_{eff}, the strain applied to the SL does not exert a pronounced influence on the band gap. All in all, the metal-to-insulator transition triggered by strong electron-electron correlations imposes constraints on the permissible range of U_{eff} values that we can select to accurately model the established electronic characteristics of the 1*H* SL. In particular, when considering $U_{\text{eff}} = 1.3$ eV, it is noteworthy that the SL exhibits a consistently metallic behavior across the entire range of lattice constants examined. Moreover, we found that our DOS compares favorably with the experimental dI/dV spectra measured in Divilov *et al.* [27] (see Fig. S4 of the SM [38]). For occupied states, the theoretical DOS exhibits a peak structure at approximately −0.8 eV and a decrease in DOS up to near E_F, where another peak develops around 0.2 eV. These features can be roughly identified in the experimental dI/dV spectrum. However, the broad peak for unoccupied states in the experimental data is located at 0.4 V. This discrepancy may stem from the limitations of density functional calculations in accurately describing empty states (as also observed in other calculation schemes, see Ref. [27]). It is worth mentioning that the gap well below E_F observed in ARPES experiments [22,53] is not accurately reproduced in our calculations. While the presented results

TABLE I. Magnetic moments obtained by Bader calculations for 1*T* SL and the 1*T* counterpart in heterostructure.

Type	Mag Nb_c (μ_b)	Mag Nb_1 (μ_b)	Mag Nb_2 (μ_b)	Mag Se (μ_b)
1*T* SL	0.426	0.399	−0.004	0.179
1*T* in heterostructure	0.237	0.293	0.067	0.123

corresponded to a 1×1 structural model, test calculations considering a geometry based on the 3×3 CDW [16] exhibit similar trends (see Fig. S3 of the SM [38]). Additionally, we have calculated the work function for both structures and found negligible differences. All in all, these findings suggest that the 3×3 charge density wave on the 1*H* layer can be disregarded when studying the electronic properties of the bilayer system. Instead, the focus is primarily on the CDW of the 1*T* phase, given its significant influence on the electronic and magnetic properties. This methodology mirrors recent research conducted by Crippa *et al.* [54] and Ayania *et al.* [55], who employed a similar approach to investigate the properties of heterostructure systems comprising both 1*T* and 1*H* phases of TaS_2, characterized by similar CDW as the ones observed for $NbSe_2$. It is important to mention that the interplay between the CDWs of 1*H* and 1*T* in the heterostructure remains an open topic and would be very interesting to address in future works. However, this issue is currently constrained by computational limitations from a DFT perspective.

In the context of the 1*T* SL, we apply a methodology similar to that used for the 1*H* counterpart. However, we investigate a $\sqrt{13} \times \sqrt{13}$ unit cell configuration, which is a distinctive feature associated with the SOD.

In Fig. 2(c), we illustrate a pronounced dependence of Δ on both lattice constants and the U_{eff} interaction parameter. This dependence also translates to the magnetic properties (see Fig. S2 in the SM [38]). For instance, for small enough values of both parameters, the known insulator state and the magnetic characteristics of the 1*T* phase (SOD) are lost. This outcome aligns with previous research findings that have underscored a strong correlation between the charge transfer gap and the structural distortion linked to the SOD [56]. Particularly, the authors have emphasized the potential of applying mechanical strain as a promising strategy for the precise adjustment and fine-tuning of the charge transfer gap in this material [56]. It is noteworthy to highlight that, within the context of the 1*T* SL, an increase in strain results in a corresponding augmentation of the magnetic moment and this phenomenon may be attributed to the enhanced super-exchange interaction, as suggested by Liu *et al.*, [57].

Putting together the information gathered so far on 1*H* and 1*T* SLs, it is clear that our nuanced and balanced approach can effectively capture and describe the collective physical properties of both SL configurations. In particular, we have identified that setting the effective Hubbard interaction parameter, U_{eff}, to 1.3 eV, and the lattice constant to 3.52 Å, successfully reproduces the main characteristics of the DOS [see Figs. 2(b)–2(d)] and magnetic characteristics of both the experimental 1*T* and 1*H* phases. This choice preserves the metallic and insulating properties characteristic of each phase, respectively. For the 1*T*-SL, our calculations indicate a band gap of ≈0.18 eV, in good agreement with the experimental gap (i.e., 0.15 eV) found by Liu *et al.* [18]. Furthermore, the SOD exhibits behavior akin to that of a spin-1/2 system with the central Nb atom (Nb_c) and its nearest-neighbor Nb atom (Nb_1), and its second-nearest neighbor (Nb_2) displaying magnetic moments of $m_{Nb_c} = 0.43\ \mu_B$, $m_{Nb_1} = 0.40\ \mu_B$ (in total), $m_{Nb_2} \approx 0\mu_B$ (in total), respectively (see Table I).

It is worth nothing that the selected lattice constant exhibits minimal dispersion, with a variation of less than 1% compared to the optimal values, being 3.49Å for 1*H* and 3.50 Å for 1*T*. Furthermore, these chosen lattice constants align well with experimental measurements (i.e., 348±14 pm and 343±11 pm for 1*H* and 1*T*, respectively) [58]. In our case, the equilibrium lattice constants for the 1*H* and 1*T* phases are within the range of 3.49–3.51 Å and 3.49–3.52 Å, respectively. Different DFT studies have obtained lattice constant parameters ranging from 3.45 Å to 3.48 Å for the 1*H* phase [16,17,46,53,57,59,60] and from 3.48 Å to 3.49 Å for the 1*T* phase [28,40,57,61]. The difference between our results and those previously reported is attributed to variations in the calculation schemes (see SM for more details [38]).

Additionally, we implemented linear response theory [39] and obtained for both phases an $U_{\text{eff}} = 1.1$ eV, very close to our choice of U_{eff}. This validates both the chosen value and the use of a single one for both phases.

B. Heterogeneous 1*T*/1*H* $NbSe_2$ bilayer

To determine the optimal arrangement of the 1*T*-$NbSe_2$ on 1*H*-$NbSe_2$ substrate, we explored different stacking configurations (Fig. S5 in the SM [38]). There are six high symmetry crystal stacking sequences where the 1*T* monolayer can stack on top of the 1*H* monolayer [62,63]. Figure 3(a) shows the lowest energy stacking geometry. Here, the Nb atoms in the 1*T* and 1*H* SLs lie on top of each other, and the interfacial Se atoms in the bottom layer, denoted as B1*T* within the 1*T* arrangement, align precisely with the hollow sites corresponding to the interfacial Se atoms in the top layer, designated as T1*H* within the 1*H* structure. This geometric arrangement gives rise to a hexagonal pattern when viewed from the top. The interlayer distance between the Nb atoms in 1*T* and 1*H* layers is d_{int}= 6.08 Å, consistent with the distance between planes in bulk 2*H*-$NbSe_2$ (i.e., 6.2 ± 0.1 Å) [64] while the distance between Se in the B1*T* and T1*H* layers is 2.8 Å. The cohesive energy between the layers is −4.47 eV, with the vdW contribution being −5.13 eV. The Nb-Nb distances within each layer are detailed in Table II. Within the 1*H* layer, the Nb-Nb bond lengths around the Nb of the 1*H* below the Nb_c are slightly elongated compared to the monolayer case. Hence, our calculations reveal a small periodic lattice distortion induced in the 1*H* phase.

The hexagonal stacking among Se atoms in the interface greatly enhances the interfacial wave-function overlap among them. Each Se atom within the B1*T* layer engages in hybridized interactions with its closest neighbors in the

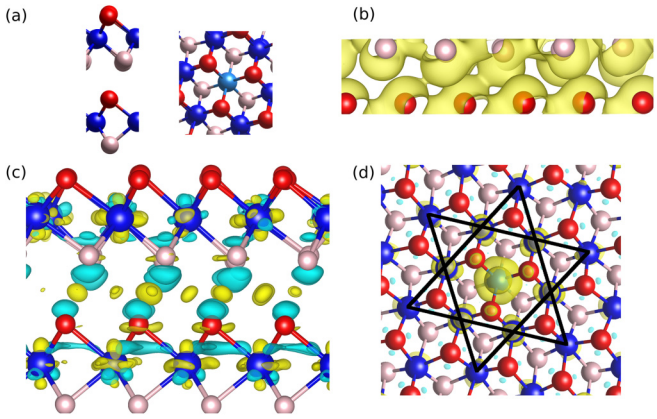

FIG. 3. Optimal stacking for the 1*T*/1*H* bilayer. (a) Schematic representation of the geometrical arrangement. In this diagram, Se atoms in the B1*T* layer are depicted as pink balls, residing in the hollow sites of the Se atoms in the T1*H* layer, shown as red balls. Additionally, Nb atoms in the 1*T* layer are positioned directly above the Nb atoms in the 1*H* layer. (b) Charge density at the interface between the Se 1*T* and 1*H* layers in the valence band (VB), with an isovalue of $10^{-5}\ e^-/\text{Å}^3$). (c) Induced charge density, $\Delta\rho = \rho_{1T\text{-}1H} - \rho_{1T} - \rho_{1H}$, representing the difference in charge density between the 1*T*/1*H* bilayer and the individual 1*T* and 1*H* layers (isovalue= $7 \times 10^{-4}\ e^-/\text{Å}^3$). Yellow and cyan represent charge accumulation and depletion, respectively. (d) Spin density distribution within the 1*T* section of the bilayer (isovalue= $1.5 \times 10^{-3}\ e^-/\text{Å}^3$).

T1*H* layer, as visually depicted in Fig. 3(b). This bonding interaction results in the emergence of interlayer bonds that exhibit characteristics akin to covalentlike quasibonds [65]. Such interlayer bonding behavior has been observed in other bilayer systems as well, as referenced in prior works [65]. These results serve as a distinctive hallmark of the interlayer interactions occurring between the 1*T* and 1*H* layers.

The interlayer interaction is thoroughly elucidated through a comprehensive analysis of the charge transfer process between the 1*T* and 1*H* arrangements, as visualized in Fig. 3(c) and summarized in Table III. This investigation reveals a charge transfer and reorganization when comparing the monolayers to the newly constructed bilayer structure. In particular, the central Nb_c atom within the 1*T* phase, and to a somewhat lesser extent the neighboring Nb_1 atoms, exhibit a marginal decrease in charge, with charge variations per atom quantifying at less than 0.01 *e*. The external Nb atoms of the SOD accumulate a marginal charge of $\approx 0.01\ e$ per atom. All in all, the net change in the overall charge of the Nb layer within the 1*T* phase amounts to a mere increment of $\approx 0.01\ e$. Notably, the lower Se atoms within the 1*T* phase experience a charge loss approximately five times more significant than their upper counterparts within the same phase, resulting in a net charge reduction of 0.18 *e* within the Se layers of the 1*T* phase. Consequently, a charge transfer of 0.17 *e* is observed, flowing from the 1*T* phase to the 1*H* phase. This is in line with our expectations, as it is consistent with the reduced work function of the 1*T* phase, $W_f^{1T} = 5.21$ eV, relative to the 1*H* phase $W_f^{1H} = 5.36$ eV. Within the 1*H* layer, a distinct redistribution of charge is also observed. The Nb layer increases its charge by 0.27 *e*, while there is a slight charge depletion (0.10 *e*) in the Se layers. It is important to highlight that the charge transfer from the 1*T* phase to the 1*H* layer is significantly reduced when compared to the TaS_2 system, as previously documented in Crippa *et al.* [54], and this variation in the charge transfer process may lead to other distinct behaviors and outcomes.

TABLE II. Distances between different Nb atoms for the 1*T* and 1*H* SL, and for 1*T* and 1*H* in the bilayer. There is a small distortion when comparing the SL with the bilayer for the 1*T*.

Type	Nb_c-Nb_1 distance (Å)	Nb_c-Nb_2 distance (Å)
1*T* SL	3.263	5.762
1*T* in heterostructure	3.285	5.784
1*H* SL	3.520	6.092
1*H* in heterostructure	3.525	6.095

All in all, the charge transfer and reorganization processes, as outlined earlier, result in the concentration of charge at the interface between the 1*T* and 1*H* layers, with a notable emphasis on the vicinity of the Se atoms of the B1*T* and T1*H* layers [see Fig. 3(c)]. This observation aligns with the presence of interfacial states, visually exemplified in Fig. 3(b). When the 1*T* and 1*H* layers come into proximity, there is a reduction in the magnetic moment of the SOD structure, as shown in Table III. The magnetic moments are as follows: $m_{\text{Nb}_c} = 0.24\ \mu_B$, $m_{\text{Nb}_1} = 0.29\ \mu_B$ (in total), $m_{\text{Nb}_2} = 0.07\ \mu_B$ (in total). Similar to the SL case, the magnetic moment of the SOD structure primarily originates from the Nb(d_{z^2}) states of the Nb_c and Nb_1 atoms, as shown in Fig. 3(d). The total magnetic moment of these states decreases from $0.72\ \mu_B$ in the 1*T*-SL configuration to $0.43\ \mu_B$ in the 1*T*-BL configuration, explaining the reduction in the total magnetic moment of the SOD structure by approximately $0.3\ \mu_B$ (from $1\ \mu_B$ to $0.72\ \mu_B$).

The electronic hybridization of interfacial Se atoms and the charge transfer processes among the layers are pivotal factors that significantly influence the electronic structures of the entire system, contrasting with the properties of their isolated components.

In the SL-1*T*, as depicted in Fig. 4(a), the valence band and the lower Hubbard band (LHB) are known to undergo hybridization, resulting in a broad peak [66], which, in our specific study, is centered at −0.22 eV. This hybridization arises from the significant overlap of the Sep_z states within the valence band with the LHB [66]. The complex interplay of these electronic states poses a substantial challenge when it comes to precisely determining the position of the LHB. In contrast, the upper Hubbard band (UHB) in the 1*T*-SL exhibits a well-defined, narrow peak, which, in our investigation, is centered at 0.11 eV.

When we contrast the SL-1*T* with its bilayer counterpart [as depicted in Fig. 4(b)], the previously observed broad peak at −0.22 eV undergoes a notable transformation, resolving into two distinct smaller peaks. The peak at −0.14 eV displays clear spin-polarized characteristics, primarily stemming from the involvement of Nb(d_{z^2}) and Se(p_z) orbitals [see Figs. 4(b) and 4(c)]. Notably, the contribution from the Nb_c SOD center

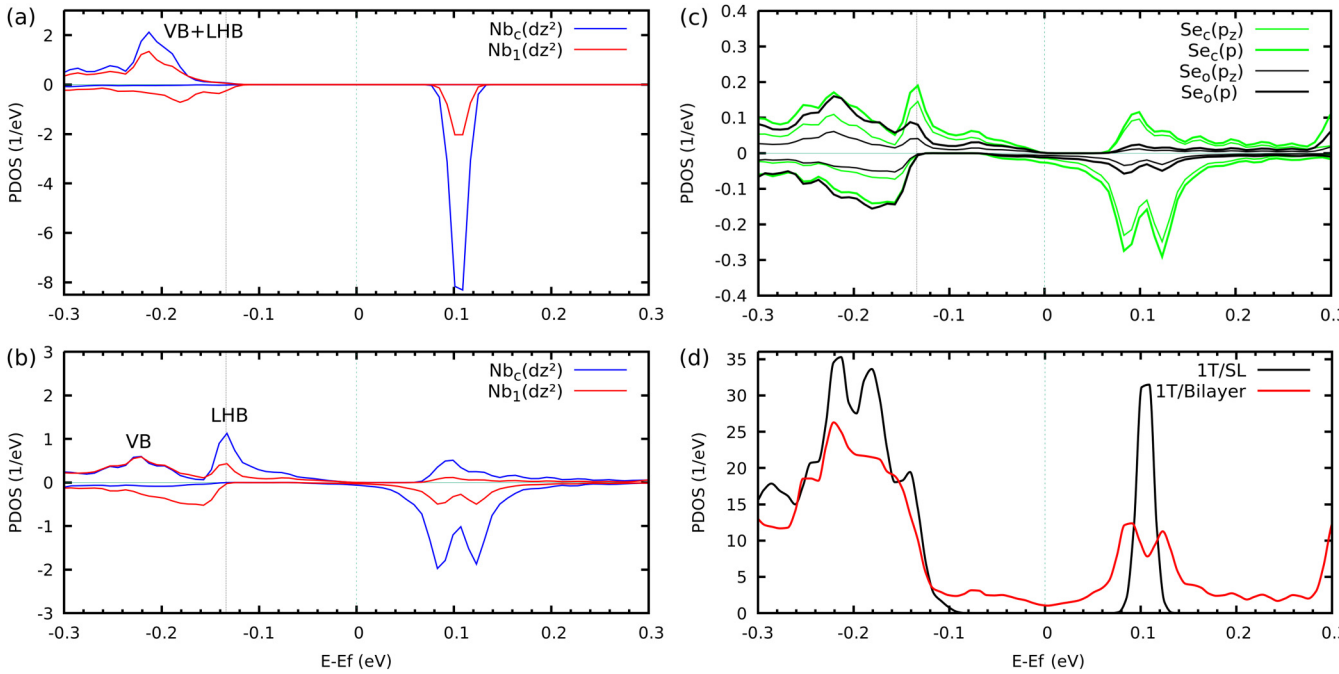

FIG. 4. Projected density of states (PDOS) into the Nb$_c(dz^2)$ (in blue) and (in red) states in both the single layer (a) and bilayer (b) configurations. Additionally, (c) illustrates the PDOS into the Se$_c(p)$ (thick green line), Se$_c(p_z)$ (thin green line), Se$_o(p)$ (thick black line), and Se$_o(p_z)$ (thin black line) states. In (a)–(c), the reported data is normalized per atom. (d) Full PDOS encompassing all atoms within the 1*T*-SL (in black) and the 1*T* part of the bilayer (in red).

exceeds that of its nearest-neighbor Nb atoms, Nb$_1$. These distinct features are also evident in the spatial distribution of the energy-resolved charge density (see Fig. S6 in the SM [38]). On the contrary, the peak positioned at −0.22 eV displays a diminished degree of spin polarization, embodying a more hybridized character. In this instance, Nb$_c$ and its nearest-neighbor Nb atoms contribute almost equally, a trend consistently evident in the corresponding energy-resolved charge density (refer to Fig. S6 in the SM [38]). Notably, this particular electronic structure spans a broader energy range, with a distinct and substantial contribution originating from Se(p_z) orbitals. All in all, our calculations suggest that the combined VB and LHB in the 1*T*-SL undergo a distinct separation when the 1*T* layer is in close proximity to the 1*H* layer. Specifically, the peak centered at −0.14 eV predominantly exhibits LHB characteristics, while the structure with a central energy of −0.22 eV displays a more pronounced VB character.

The UHB in our observations also undergoes substantial alterations when compared to the SL case. Notably, we have observed that the UHB peak broadens and separates into two distinct components. The exact cause of this splitting remains unclear, as both peaks exhibit significant contributions from Nb$_c(d_{z^2})$ states, along with contributions from their nearest neighbors (as evidenced in Fig. 4(b) and further illustrated in Fig. S6 in the SM [38]).

To further support the assignment of the LHB, VB and UHB we conducted a series of calculations using different U_{eff} parameters within our DFT+U framework. These calculations provided valuable insights into the behavior of these bands. Specifically, we observed that the peak associated with the LHB shifts towards lower energies, and the gap between the LHB and UHB increases as the U_{eff} values are elevated, in line with our expectations. Intriguingly, we also found that the splitting of the UHB is influenced by the U_{eff} parameter (for detailed visualization, refer to Fig. S8 in the SM [38]).

The preceding discussion highlights the significant impact of the proximity between the 1*T* and 1*H* layers on the behavior of the LHB and UHB, resulting in their shifting closer to the Fermi level. This observed phenomenon can be attributed

TABLE III. Bader charge transfer analysis was performed for the 1*T*/1*H* bilayer, yielding values of Δ_q(Nb) and Δ_q(Se), which represent the total charge transferred for all Nb and Se atoms, respectively, in either the 1*T* or 1*H* component of the heterobilayer relative to the isolated monolayers. Additionally, the magnetic moment changes in Nb and Se atoms for the 1*T* or 1*H* components of the bilayer with respect to the isolated monolayers are represented by Δ_m(Nb) (μ_B) and Δ_m (μ_B), respectively. The value corresponding to the center of the SOD is given for the 1*T* component, while the average value for all atoms is given for the other cases.

Species	Δ_q(Nb) (e$^-$)	Δ_q(Se) (e$^-$)	Δ_m(Nb) (μ_B)	Δ_m(Se) (μ_B)
1*T*	0.014 (total)	−0.180 (total)	−0.189 (Nb$_c$)	≈ 0 (average)
1*H*	0.273 (total)	−0.107 (total)	−0.106 (average)	≈ 0 (average)

to the dielectric screening effects originating from the lower layer acting on the uppermost layer. This dielectric screening effectively reduces the on-site Coulomb repulsion (Hubbard U), thereby decreasing the energy gap between the LHB and the UHB [67]. As a direct consequence of the reduction in U, a decrease in the charge within the majority spin is observed, along with an increase in the occupation of the $Nb_c(d_{z^2})$ and states in the minority spin. Importantly, this shift in charge distribution occurs while the overall total charge of the states remains relatively unchanged. This phenomenon serves to elucidate the underlying cause of the decrease in the magnetic moment of the SOD structure (additional details available in Fig. S9 of the SM [38]).

The reduced on-site Coulomb repulsion U effectively decreases the gap between the Hubbard bands. In conjunction with their hybridization with the valence band, this leads to broadening, reduced localization, and extended tails. These effects contribute to the emergence of states at the Fermi level, consistent with the 1T phase's transition towards a metallic phase. Evidence of this is seen in the PDOS for the 1T whole arrangement, as depicted in Fig. 4(d). The orbital composition of these states not only involves atoms and orbitals that are directly associated with the Hubbard bands. This observation strongly reinforces the idea that the overall system, rather than the Hubbard bands in isolation, plays a pivotal role in accounting for the population of these states and, consequently, for the insulating-to-metallic transition within the 1T phase in the bilayer system. This transition is a direct result of the proximity effect induced by the metallic 1H counterpart, reflecting the intricate interplay of electronic interactions within the system.

In summary, our findings indicate that the magnetic moment of the SOD persists within the heterostructure, which is an essential ingredient for the Kondo effect, as experimentally revealed by [18]. Additionally, the 1T phase itself develops metallicity. We also find evidence of hybridization between the 1T and 1H layers, along with a reduction in the effective Coulomb interaction, U, within the lower Hubbard band and upper Hubbard band. The metallicity of the 1T phase in the bilayer could be observed in experiments conducted above the Kondo temperature. At very low temperatures, when the 1H phase becomes superconducting (an effect not captured by DFT calculations), our results suggest that this superconductivity could be induced in the 1T phase due to interlayer coupling. Both the Kondo effect and the Yu-Shiba-Rusinov resonances observed in experiments require significant coupling between the magnetic moment and the host. Until now, this coupling was thought to occur exclusively between the 1T and 1H layers. However, our study suggests that such coupling could occur within the 1T layer itself, potentially leading to much higher hybridization. The occurrence of Kondo effect, and even of a Kondo lattice behavior, due to metallicity developed within a 1T-stripe phase has already been reported in Liu *et al.* [68]. Finally, our systematic study of charge transfer between the layers provides insights into how they interact and preserve or modify their character in the heterostructure.

IV. CONCLUSIONS

In this theoretical investigation, we conducted a comprehensive study of 1T-$NbSe_2$ and 1H-$NbSe_2$ SLs and their 1T/1H heterobilayer structure by means of DFT calculations. Our findings indicate that a $U_{\text{eff}} = 1.3$ eV and a lattice constant of 3.52 Å adequately describe the overall physical properties of both SLs configurations, providing a common framework for both phases. This unified setup is essential for investigating the properties of the heterobilayer system. For the 1T/1H heterobilayer, we explored the interlayer interaction between the SLs. Our investigation found a charge transfer and reorganization process between 1T and 1H layers of 0.17 e flowing from the 1T phase to the 1H phase and supported by work function calculations. In particular, there is a concentration of charge at the interface between the 1T and 1H layers, primarily in the vicinity of the Se atoms. This localized charge accumulation gives rise to the presence of interfacial states. Upon bringing the 1T and 1H layers into close proximity, a reduction in the magnetic moment of the SOD structure is observed, decreasing 0.3 μ_B, while still maintaining its presence, which is a key ingredient for the Kondo effect observed in experiments. In the 1T-SL, the VB and the LHB undergo hybridization, forming a broad peak. When the two SLs come into contact, this peak splits into two distinct structures: one with clear LHB attributes and another with reduced spin polarization and more hybridized character. Additionally, the UHB broadens. This transformation in the electronic structure near the Fermi level is accompanied by a reduction in the Hubbard U due to the dielectric screening effect between the layers. The combined effects of reduced effective Hubbard U and hybridization between the single layers play a crucial role in the emergence of metallic states in the 1T/1H heterobilayer.

All data that support the findings of this paper are included within the article (and any SM files).

ACKNOWLEDGMENTS

R.P., I. H., and P.A. acknowledge the financial support from CONICET PIP-0883 and the computational time provided by the CCT-Rosario computational center and Computational Simulation Center (CSC) for Technological Applications, members of the High Performance Computing National System (SNCAD-MincyT Argentina). This work was also supported by Ministerio de Ciencia Innovación y Universidades through Project PID2021-127917NB-I00 by MCIN AEI/10.13039/501100011033, as well as by project IT-1527-22 funded by the Basque Government, and No. 202260I187 funded by CSIC.

[1] K. S. Novoselov, A. Mishchenko, A. Carvalho, and A. H. C. Neto, 2D materials and van der Waals heterostructures, Science **353**, aac9439 (2016).

[2] A. K. Geim and I. V. Grigorieva, Van der Waals heterostructures, Nature (London) **499**, 419 (2013).

[3] M. Bernardi, C. Ataca, M. Palummo, and J. C. Grossman, Optical and electronic properties of two-dimensional layered materials, Nanophotonics **6**, 479 (2017).

[4] P. Darancet, A. J. Millis, and C. A. Marianetti, Three-dimensional metallic and two-dimensional insulating behavior

in octahedral tantalum dichalcogenides, Phys. Rev. B **90**, 045134 (2014).
[5] T. Ritschel, J. Trinckauf, B. B. K. Koepernik, M. v. Zimmermann, H. Berger, P. A. Y. I. Joe, and J. Geck, Orbital textures and charge density waves in transition metal dichalcogenides, Nat. Phys. **11**, 328 (2015).
[6] T. Ritschel, H. Berger, and J. Geck, Stacking-driven gap formation in layered 1*T*-TaS_2, Phys. Rev. B **98**, 195134 (2018).
[7] J. W. Park, J. Lee, and H. W. Yeom, Zoology of domain walls in quasi-2D correlated charge density wave of 1*T*-TaS_2, npj Quantum Mater. **6**, 32 (2021).
[8] J. Jung, J. W. Park, J. Kim, and H. W. Yeom, Surface enhanced electron correlation on the trivial quasi-two-dimensional bulk insulator 1*T*-TaS_2, Phys. Rev. B **106**, 155406 (2022).
[9] C. J. Sayers, G. Cerullo, Y. Zhang, C. E. Sanders, R. T. Chapman, A. S. Wyatt, G. Chatterjee, E. Springate, D. Wolverson, E. Da Como, and E. Carpene, Exploring the charge density wave phase of 1*T*-$TaSe_2$: Mott or charge-transfer gap? Phys. Rev. Lett. **130**, 156401 (2023).
[10] Y. Chen, W. Ruan, M. Wu, S. Tang, H. Ryu, H.-Z. Tsai, R. L. Lee, S. Kahn, F. Liou, C. Jia, O. R. Albertini, H. Xiong, T. Jia, Z. Liu, J. A. Sobota, A. Y. Liu, J. E. Moore, Z.-X. Shen, S. G. Louie, S.-K. Mo *et al.*, Strong correlations and orbital texture in single-layer 1*T*-$TaSe_2$, Nat. Phys. **16**, 218 (2020).
[11] W. Ruan, Y. Chen, S. Tang, J. Hwang, H.-Z. Tsai, R. L. Lee, M. Wu, H. Ryu, S. Kahn, F. Liou, C. Jia, A. Aikawa, C. Hwang, F. Wang, Y. Choi, S. G. Louie, P. A. Lee, Z.-X. Shen, S.-K. Mo, and M. F. Crommie, Evidence for quantum spin liquid behaviour in single-layer 1*T*-$TaSe_2$ from scanning tunnelling microscopy, Nat. Phys. **17**, 1154 (2021).
[12] W. Wang, C. Si, W. Lei, F. Xiao, Y. Liu, C. Autieri, and X. Ming, Stacking order and coulomb correlation effect in the layered charge density wave phase of 1*T*-NbS_2, Phys. Rev. B **105**, 035119 (2022).
[13] W. Wang, B. Wang, Z. Gao, G. Tang, W. Lei, X. Zheng, H. Li, X. Ming, and C. Autieri, Charge density wave instability and pressure-induced superconductivity in bulk 1*T*-NbS_2, Phys. Rev. B **102**, 155115 (2020).
[14] X. Xi, Z. Wang, W. Zhao, J.-H. Park, K. T. Law, H. Berger, L. Forró, J. Shan, and K. F. Mak, Ising pairing in superconducting $NbSe_2$ atomic layers, Nat. Phys. **12**, 139 (2016).
[15] M. M. Ugeda, A. J. Bradley, Y. Zhang, S. Onishi, Y. Chen, W. Ruan, C. Ojeda-Aristizabal, H. Ryu, M. T. Edmonds, H.-Z. Tsai, A. Riss, S.-K. Mo, D. Lee, A. Zettl, Z. Hussain, Z.-X. Shen, and M. F. Crommie, Characterization of collective ground states in single-layer $NbSe_2$, Nat. Phys. **12**, 92 (2016).
[16] B. Guster, C. Rubio-Verdú, R. Robles, J. Zaldívar, P. Dreher, M. Pruneda, J. Á. Silva-Guillén, D.-J. Choi, J. I. Pascual, M. M. Ugeda, P. Ordejón, and E. Canadell, Coexistence of elastic modulations in the charge density wave state of 2*H*-$NbSe_2$, Nano Lett. **19**, 3027 (2019).
[17] C.-S. Lian, C. Si, and W. Duan, Unveiling charge-density wave, superconductivity, and their competitive nature in two-dimensional $NbSe_2$, Nano Lett. **18**, 2924 (2018).
[18] M. Liu, J. Leveillee, S. Lu, J. Yu, H. Kim, C. Tian, Y. Shi, K. Lai, C. Zhang, F. Giustino, and C.-K. Shih, Monolayer 1*T*-$NbSe_2$ as a 2D-correlated magnetic insulator, Sci. Adv. **7**, eabi6339 (2021).
[19] R. F. Frindt, Superconductivity in ultrathin $NbSe_2$ layers, Phys. Rev. Lett. **28**, 299 (1972).
[20] N. E. Staley, J. Wu, P. Eklund, Y. Liu, L. Li, and Z. Xu, Electric field effect on superconductivity in atomically thin flakes of $NbSe_2$, Phys. Rev. B **80**, 184505 (2009).
[21] A. Hamill, B. Heischmidt, E. Sohn, D. Shaffer, K.-T. Tsai, X. Zhang, X. Xi, A. Suslov, H. Berger, L. Forró, F. J. Burnell, J. Shan, K. F. Mak, R. M. Fernandes, K. Wang, and V. S. Pribiag, Two-fold symmetric superconductivity in few-layer $NbSe_2$, Nat. Phys. **17**, 949 (2021).
[22] Y. Nakata, K. Sugawara, S. Ichinokura, Y. Okada, T. Hitosugi, T. Koretsune, K. Ueno, S. Hasegawa, T. Takahashi, and T. Sato, Anisotropic band splitting in monolayer $NbSe_2$: Implications for superconductivity and charge density wave, npj 2D Mater. Appl. **2**, 12 (2018).
[23] Y. Nakata, K. Sugawara, R. Shimizu, Y. Okada, P. Han, T. Hitosugi, K. Ueno, T. Sato, and T. Takahashi, Monolayer 1*T*-$NbSe_2$ as a Mott insulator, NPG Asia Mater. **8**, e321 (2016).
[24] L. Liu, X. Song, X. Huang, H. Ji, Z. Hu, Y. Huang, H.-J. Gao, and Y. Wang, Review: Exploring spin properties in van der Waals materials with star-of-David pattern, Mater. Today Electron. **6**, 100068 (2023).
[25] E. Liebhaber, S. Acero González, R. Baba, G. Reecht, B. W. Heinrich, S. Rohlf, K. Rossnagel, F. von Oppen, and K. J. Franke, Yu-Shiba-Rusinov states in the charge-density modulated superconductor $NbSe_2$, Nano Lett. **20**, 339 (2020).
[26] L. Liu, X. Song, J. Dai, H. Yang, Y. Chen, X. Huang, Z. Huang, H. Ji, Y. Zhang, X. Wu, J.-T. Sun, Q. Zhang, J. Zhou, Y. Huang, J. Qiao, W. Ji, H.-J. Gao, and Y. Wang, Unveiling electronic behaviors in heterochiral charge-density-wave twisted stacking materials with 1.25 nm unit dependence, ACS Nano **17**, 2702 (2023).
[27] S. Divilov, W. Wan, P. Dreher, E. Bölen, D. Sánchez-Portal, M. M. Ugeda, and F. Ynduráin, Magnetic correlations in single-layer $NbSe_2$, J. Phys.: Condens. Matter **33**, 295804 (2021).
[28] M. Calandra, Phonon-assisted magnetic Mott-insulating state in the charge density wave phase of single-layer 1*T*-$NbSe_{22}$, Phys. Rev. Lett. **121**, 026401 (2018).
[29] G. Kresse and J. Hafner, *Ab initio* molecular dynamics for liquid metals, Phys. Rev. B **47**, 558 (1993).
[30] G. Kresse and J. Hafner, *Ab initio* molecular dynamics for open-shell transition metals, Phys. Rev. B **48**, 13115 (1993).
[31] G. Kresse and J. Furthmüller, Efficiency of *ab-initio* total energy calculations for metals and semiconductors using a plane-wave basis set, Comput. Mater. Sci. **6**, 15 (1996).
[32] G. Kresse and J. Furthmüller, Efficient iterative schemes for *ab initio* total-energy calculations using a plane-wave basis set, Phys. Rev. B **54**, 11169 (1996).
[33] G. Kresse and D. Joubert, From ultrasoft pseudopotentials to the projector augmented-wave method, Phys. Rev. B **59**, 1758 (1999).
[34] J. Hafner, *Ab-initio* simulations of materials using VASP: Density-functional theory and beyond, J. Comput. Chem. **29**, 2044 (2008).
[35] J. P. Perdew, K. Burke, and M. Ernzerhof, Generalized gradient approximation made simple, Phys. Rev. Lett. **77**, 3865 (1996).
[36] A. Tkatchenko and M. Scheffler, Accurate molecular van der Waals interactions from ground-state electron density and free-atom reference data, Phys. Rev. Lett. **102**, 073005 (2009).
[37] S. L. Dudarev, G. A. Botton, S. Y. Savrasov, C. J. Humphreys, and A. P. Sutton, Electron-energy-loss spectra and the structural

stability of nickel oxide: An LSDA + U study, Phys. Rev. B **57**, 1505 (1998).

[38] See Supplemental Material at http://link.aps.org/supplemental/10.1103/PhysRevB.110.075427 for additional computational details and results. Figure S1 provides a schematic representation of the 1T unit cell; Fig. S2 shows the evolution of the magnetic moment in comparison with the lattice parameter; Fig. S3 presents the DOS of the 1 x 1 and 3 x 3 CDW in the 1H phase; Fig. S4 displays the PDOS of the 1H phase for different values of U_{eff}; Fig. S5 illustrates different views of the stacking configurations; Fig. S6 visualizes the wave function for different bands of interest; Fig. S7 depicts the band structure for 1T-SL and 1T in the heterostructure; Fig. S8 shows the evolution of the LHB, VB, and UHB as a function of U_{eff}; Fig. S9 presents the evolution of the charge and magnetic moment as a function of the 1T/1H distance. It also contains Refs. [4,16,27,48].

[39] M. Cococcioni and S. de Gironcoli, Linear response approach to the calculation of the effective interaction parameters in the LDA + U method, Phys. Rev. B **71**, 035105 (2005).

[40] E. Kamil, J. Berges, G. Schönhoff, M. Rösner, M. Schüler, G. Sangiovanni, and T. O. Wehling, Electronic structure of single layer 1T-$NbSe_2$: interplay of lattice distortions, non-local exchange, and Mott–Hubbard correlations, J. Phys.: Condens. Matter **30**, 325601 (2018).

[41] M. Yu and D. R. Trinkle, Accurate and efficient algorithm for Bader charge integration, J. Chem. Phys. **134**, 064111 (2011).

[42] S. C. de la Barrera, M. R. Sinko, D. P. Gopalan, N. Sivadas, K. L. Seyler, K. Watanabe, T. Taniguchi, A. W. Tsen, X. Xu, D. Xiao, and B. M. Hunt, Tuning Ising superconductivity with layer and spin–orbit coupling in two-dimensional transition-metal dichalcogenides., Nat. Commun. **9**, 1427 (2018).

[43] J. Á. Silva-Guillen, P. Ordejon, F. Guinea, and E. Canadell, Electronic structure of 2H-$NbSe_2$ single-layers in the CDW state, 2D Mater. **3**, 035028 (2016).

[44] G. Gye, E. Oh, and H. W. Yeom, Topological landscape of competing charge density waves in 2H-$NbSe_2$, Phys. Rev. Lett. **122**, 016403 (2019).

[45] E. Oh, G. Gye, and H. W. Yeom, Defect-selective charge-density-wave condensation in 2H-$NbSe_2$, Phys. Rev. Lett. **125**, 036804 (2020).

[46] F. Cossu, A. G. Moghaddam, K. Kim, H. A. Tahini, I. Di Marco, H.-W. Yeom, and A. Akbari, Unveiling hidden charge density waves in single-layer $NbSe_2$ by impurities, Phys. Rev. B **98**, 195419 (2018).

[47] U. Chatterjee, J. Zhao, M. Iavarone, R. Di Capua, J. P. Castellan, G. Karapetrov, C. D. Malliakas, M. G. Kanatzidis, H. Claus, J. P. C. Ruff, F. Weber, J. van Wezel, J. C. Campuzano, R. Osborn, M. Randeria, N. Trivedi, M. R. Norman, and S. Rosenkranz, Emergence of coherence in the charge-density wave state of 2H-$NbSe_2$, Nat. Commun. **6**, 6313 (2015).

[48] D. Wickramaratne, S. Khmelevskyi, D. F. Agterberg, and I. I. Mazin, Ising superconductivity and magnetism in $NbSe_2$, Phys. Rev. X **10**, 041003 (2020).

[49] It is also worth commenting that in the case of $NbSe_2$, the 1T phase does not naturally occur in bulk crystals; rather, it was discovered to coexist with the 1H phase during the molecular beam epitaxy growth of monolayer $NbSe_2$ on graphene.

[50] Y. Chen, L. Liu, X. Song, H. Yang, Z. Huang, T. Zhang, H. Yang, H.-J. Gao, and Y. Wang, Twisted charge-density-wave patterns in bilayer 2D crystals and modulated electronic states, 2D Mater. **9**, 014007 (2022).

[51] Q. Zhang, Y. Hou, T. Zhang, Z. Xu, Z. Huang, P. Yuan, L. Jia, H. Yang, Y. Huang, W. Ji, J. Qiao, X. Wu, and Y. Wang, Visualizing spatial evolution of electron-correlated interface in two-dimensional heterostructures, ACS Nano **15**, 16589 (2021).

[52] Z.-Y. Liu, S. Qiao, B. Huang, Q.-Y. Tang, Z.-H. Ling, W.-H. Zhang, H.-N. Xia, X. Liao, H. Shi, W.-H. Mao, G.-L. Zhu, J.-T. Lü, and Y.-S. Fu, Charge transfer gap tuning via structural distortion in monolayer 1T-$NbSe_2$, Nano Lett. **21**, 7005 (2021).

[53] C.-Z. Xu, X. Wang, P. Chen, D. Flötotto, J. A. Hlevyack, M.-K. Lin, G. Bian, S.-K. Mo, and T.-C. Chiang, Experimental and theoretical electronic structure and symmetry effects in ultrathin $NbSe_2$ films, Phys. Rev. Mater. **2**, 064002 (2018).

[54] L. Crippa, H. Bae, P. Wunderlich, I. I. Mazin, B. Yan, G. Sangiovanni, T. Wehling, and R. Valentí, Heavy fermions vs doped Mott physics in heterogeneous Ta-dichalcogenide bilayers, Nat. Commun. **15**, 1357 (2024).

[55] C. G. Ayani, M. Bosnar, F. Calleja, A. P. Solé, O. Stetsovych, I. M. Ibarburu, C. Rebanal, M. Garnica, R. Miranda, M. M. Otrokov, M. Ondráček, P. Jelínek, and A. Arnau, Unveiling the interlayer interaction in a 1H/1T TaS_2 van de Waals heterostructure, Nano Lett. (2024), doi:10.1021/acs.nanolett.4c02068.

[56] Y. Liu, Y. Huang, and X. Duan, Van der Waals integration before and beyond two-dimensional materials, Nature (London) **567**, 323 (2019).

[57] Y. Liu, Y. Feng, L. Hu, X. Wu, S. Qiao, and G. Gao, Structural, electronic phase transitions and thermal spin transport properties in 2D $NbSe_2$ and NbS_2: A first-principles study, Phys. Chem. Chem. Phys. **25**, 1632 (2023).

[58] Z. Huang, X. Song, Y. Chen, H. Yang, P. Yuan, H. Ma, J. Qiao, Y. Zhang, J. Sun, T. Zhang, Y. Huang, L. Liu, H.-J. Gao, and Y. Wang, Size dependence of charge-density-wave orders in single-layer $NbSe_2$ hetero/homophase junctions, J. Phys. Chem. Lett. **13**, 1901 (2022).

[59] F. Cossu, K. Palotás, S. Sarkar, I. D. Marco, and A. Akbari, Strain-induced stripe phase in charge-ordered single layer $NbSe_2$, NPG Asia Mater. **12**, 24 (2020).

[60] F. Zheng, Z. Zhou, X. Liu, and J. Feng, First-principles study of charge and magnetic ordering in monolayer $NbSe_2$, Phys. Rev. B **97**, 081101(R) (2018).

[61] D. Pasquier and O. V. Yazyev, Charge density wave phase, Mottness, and ferromagnetism in monolayer 1T-$NbSe_2$, Phys. Rev. B **98**, 045114 (2018).

[62] S. Kezilebieke, M. N. Huda, P. Dreher, I. Manninen, Y. Zhou, J. Sainio, R. Mansell, M. M. Ugeda, S. van Dijken, H.-P. Komsa, and P. Liljeroth, Electronic and magnetic characterization of epitaxial VSe_2 monolayers on superconducting $NbSe_2$, Commun. Phys. **3**, 116 (2020).

[63] X. Hu, Y. Wang, X. Shen, A. V. Krasheninnikov, L. Sun, and Z. Chen, 1T phase as an efficient hole injection layer to TMDS transistors: a universal approach to achieve p-type contacts, 2D Mater. **5**, 031012 (2018).

[64] H. Zhang, A. Rousuli, K. Zhang, L. Luo, C. Guo, X. Cong, Z. Lin, C. Bao, H. Zhang, S. Xu, R. Feng, S. Shen, K. Zhao, W. Yao, Y. Wu, S. Ji, X. Chen, P. Tan, Q.-K. Xue, Y. Xu *et al.*,

Tailored Ising superconductivity in intercalated bulk $NbSe_2$, Nat. Phys. **18**, 1425 (2022).

[65] J. Dai, J. Qiao, C. Wang, L. Zhou, X. Wu, L. Liu, X. Song, F. Pang, Z. Cheng, X. Kong, Y. Wang, and W. Ji, Layer sliding and twisting induced electronic transitions in correlated magnetic 1*T*-$NbSe_2$ bilayers, Adv. Funct. Mater. **33**, 2302989 (2023).

[66] L. Liu, H. Yang, Y. Huang, X. Song, Q. Zhang, Z. Huang, Y. Hou, Y. Chen, Z. Xu, T. Zhang, X. Wu, J. Sun, Y. Huang, F. Zheng, X. Li, Y. Yao, H.-J. Gao, and Y. Wang, Direct identification of Mott Hubbard band pattern beyond charge density wave superlattice in monolayer 1*T*-$NbSe_2$, Nat. Commun. **12**, 1978 (2021).

[67] A similar reduction, attributed to the addition of extra layers, was also observed in 1*T*-$TaSe_2$[10].

[68] Z.-Y. Liu, H. Jin, Y. Zhang, K. Fan, T.-F. Guo, H.-J. Qin, L.-F. Zhu, L.-Z. Yang, W.-H. Zhang, B. Huang, and Y.-S. Fu, Charge-density wave mediated quasi-one-dimensional Kondo lattice in stripe-phase monolayer 1*T*-$NbSe_2$, Nat. Commun. **15**, 1039 (2024).